Special Issue: Design and Control Technologies for Intelligent Vehicle Systems

Journal of Vibration and Control
2021, Vol. 0(0) 1–16

DOI: 10.1177/10775463211002619
journals.sagepub.com/home/jvc
SAGE

String stable control of electric heavy vehicle platoon with varying battery pack locations

K B Devika[1], G Rohith[2], and Shankar C Subramanian[1]

Abstract

Integration of heavy commercial road vehicle platooning concept and electric vehicle technology is a promising approach as far as sustainable freight transportation is considered. This article attempts to design a string stable controller for an electric heavy commercial road vehicle platoon by incorporating critical factors such as complete vehicle dynamics model, pneumatic brake system model and cooperative braking between friction and regenerative braking systems. The sliding mode control technique has been used for string stable platoon operation. The impact of various battery pack locations on string stability has also been analysed. The performance of the controller has been investigated by considering electric heavy commercial road vehicle platoon operation on different road slope (straight, uphill and downhill) conditions, dry and wet road conditions and vehicle load conditions. It has been observed that the battery pack location has a significant influence on string stability with respect to the platoon operating conditions. During operation on straight and level roads, string stability was achieved irrespective of the location of the battery pack. However, during downhill and uphill driving conditions, it was found that placing the battery pack near front and rear axle locations, respectively, helped in ensuring string stable platoon operation.

Keywords

Battery position, electric vehicle, heavy commercial road vehicle, platoon, string stability

1. Introduction

A perfect balance between environmental and business sustainability has become an important objective of the present day automotive research community. With increasing focus on economic freight transportation, it is equally imperative to give emphasis on decarbonisation strategies (Teoh et al., 2018; Mulholland et al., 2018). Vehicle platooning is a promising technique that can considerably reduce fuel consumption while operating heavy vehicle fleets for freight movement (Chehardoli and Ghasemi, 2019). This would also result in maximum utilisation of available road infrastructure. However, large-scale decarbonisation is not possible as long as conventional heavy vehicles are relied upon for freight transportation via vehicle platooning. In this regard, the concept of electric vehicle (EV) platooning gains significant interest. EVs are known for their capability to ensure reduced emission, leaving behind minimal carbon footprints (Wu et al., 2019; Cano et al., 2018). Considering all these factors, the realisation of autonomous electric Heavy Commercial Road Vehicle (HCRV) platoons can be considered as an economical and environmental sustainable solution for future freight movement. However, practical realisation of such platoons would encounter several technical challenges; one among them is ensuring the string stability of vehicular platoons.

In a vehicular platoon, under the assumption that the initial disturbances/perturbations are bounded, if the spacing errors between all the vehicles are bounded uniformly in time, then the platoon is said to be 'string stable' (Swaroop et al., 1994; Swaroop, 1997). This could be achieved by maintaining uniform longitudinal speed by the vehicles in the platoon and also by maintaining constant inter-vehicular spacing between the vehicles. It is extremely important to establish string stable operation to have a safe and collision-free autonomous operation of vehicular platoons. Hence, a controller that could establish

[1]Department of Engineering Design, IIT Madras, India
[2]Department of Mechanical Engineering, IIT Gandhinagar, India

Received: 30 September 2020; accepted: 23 February 2021

Corresponding author:
Shankar C. Subramanian, Engineering Design Department, IIT Madras, Chennai, Tamil Nadu 600036, India.
Email: shankarram@iitm.ac.in.

string stability is a crucial requirement for the autonomous operation of a vehicle platoon (Chehardoli, 2020a, 2020b).

Platooning concepts for conventional heavy vehicles have been thoroughly investigated by the automotive research fraternity. A distributed approach using a network of controllers has been presented in Larson et al. (2014) so as to maximise the amount of fuel saved by coordinating platoon formation. In Alam et al. (2015), a detailed description on heavy vehicle platooning and the potential use of heavy vehicle platooning as a solution for sustainable freight transportation have been presented. A cooperative look-ahead control framework for fuel-efficient and safe heavy-duty vehicle platoon operation has been presented in Turri et al. (2016). String stable controller design for heavy vehicle platoons using a variable time headway approach has been presented in Yanakiev and Kanellakopoulos (1995). The effects of pneumatic actuation delay on string stability of heavy vehicle platoons have been investigated in Devika et al. (2019). A fuel-efficient heavy vehicle platoon control scheme using disturbance observer has been reported in Na et al. (2020).

With the penetration of EV technology, the automotive research community is now more focused on sustainable transportation solutions. In this regard, one could pose electric HCRV platoon as a viable and sustainable solution. In Kaluva et al. (2020), the fuel efficiency of autonomous electric cars has been investigated through aerodynamic drag analysis. A model predictive control–based hybrid EV platooning using slope information and route information has been presented in Yu et al. (2016a, 2016b), respectively. However, these studies dealt with the platooning of electric/hybrid electric cars.

While dealing with HCRVs, in contrast with passenger cars, additional challenges such as pneumatic actuation delay, mass variation during laden and unladen operating conditions and higher dynamic load transfer during braking have to be considered when designing string stable controllers. Particularly, while one considers electric HCRV platoons, the above-mentioned factors are more significant because of the additional components such as battery pack and motors. The additional mass contributions from these electrical components may significantly affect the stability of the vehicle and also the platoon string stability as a whole. In addition, the battery pack positioning in EVs would affect drive comfort as well as vehicle stability (Suriyamoorthy et al., 2019). Placing the battery pack at different locations would affect the load distribution and hence could have an impact on the platoon stability. Also, in addition to pneumatic brake system delay in heavy vehicles, the dynamic traction in motor response characteristics in individual electric HCRVs may affect the platoon string stability. These factors have been considered in this article to realise electric HCRV platoons. Inclusion of these factors makes the vehicle dynamics model nonlinear. Hence, sliding mode control (SMC), which is a well-established nonlinear control strategy (Utkin, 1977), has been used for string stable controller design. To deal with chattering problem (high-frequency control signal switching) in SMC and to ensure robust control action, a Power Rate Exponential Reaching Law (PRERL) (Devika and Thomas, 2017)–based SMC design has been used in this article.

To mirror real vehicle operating conditions, a detailed EV dynamics model encompassing resistive forces, tyre model and wheel dynamics has been used for string stable controller design and stability analysis. Transfer function models that characterise the pneumatic brake system and electric motor system dynamics have also been incorporated in the design. A cooperative braking strategy between friction braking and regenerative braking has suitably been used to realise braking scenarios in electric HCRVs.

The primary focus of this work is to design a string stable controller for an electric HCRV platoon considering the aforementioned critical factors. The major contributions of this article are the following:

1. A string stable controller has been designed for electric HCRV platoons considering complete vehicle dynamics model with resistive forces, tyre model and wheel dynamics.
2. The design also considered the electric motor dynamics and the pneumatic brake system dynamics, thus incorporating the complete actuation dynamics in electric HRCVs.
3. The string stable controller has been designed based on the PRERL–based SMC strategy, which is capable of mitigating chattering, whereas providing sufficient robustness.
4. A parallel cooperative braking strategy has been used in the design for characterising braking in electric HCRVs.
5. The impact of different battery pack locations on the string stability of electric HCRV platoon has been investigated.
6. The performance of the string stable controller and the effects of placing the battery pack at different positions under different operating conditions have been analysed.
7. The importance of using a dynamic model for controller design has been illustrated by comparing the controller performance with one that is based on a kinematic model.

The overall design framework for the electric HCRV platoon considered in this study is detailed in Figure 1. The considered platoon consists of $N + 1$ electric HCRVs, with one leader and N followers. The major assumptions made in this study are the following:

1. Only the longitudinal dynamics of the vehicle is considered.

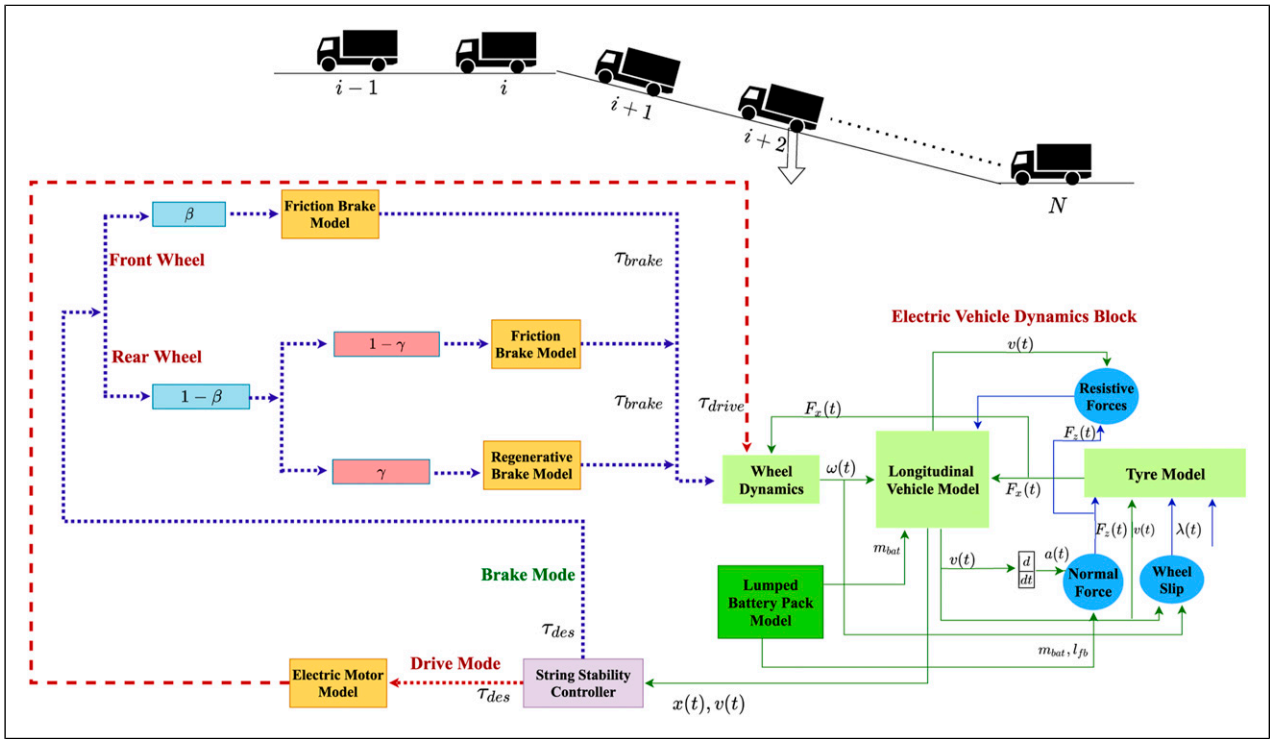

Figure 1. Electric heavy commercial road vehicle platoon – design framework.

2. The tyre model and vehicle parameters are assumed to be known.
3. Equal distribution of load is assumed on the left wheel and the right wheel of the same axle.
4. A rear wheel drive hub motor configuration is considered for the electric HCRV.
5. The battery pack is at a constant height from the ground and is constrained to move only in the longitudinal direction.

2. Vehicle dynamics model

The position and speed dynamics of ith follower vehicle in the platoon can be represented as

$$\begin{aligned} \dot{x}_i(t) &= v_i(t) \\ \dot{v}_i(t) &= \Omega(v_i(t), \tau_{vi}(t)) \end{aligned} \tag{1}$$

where $i = 1 \ldots N$, and $v_i(t)$ and $\tau_{vi}(t)$ represent the longitudinal speed and drive/brake torque of the vehicle, respectively. Here, $\Omega(v_i(t), \tau_{vi}(t))$ is a nonlinear function in $v_i(t)$ and $\tau_{vi}(t)$ that can be expressed as

$$\begin{aligned} \Omega(v_i(t), \tau_{vi}(t)) = \frac{1}{m_{vi}} \big(F_{xfvi}(\lambda_{fvi}(t)) + F_{xrvi}(\lambda_{rvi}(t)) \\ - F_{Rvi}(t)\big) \end{aligned} \tag{2}$$

where m_{vi} is the mass of the ith vehicle in the platoon, $F_{xfvi}(\lambda_{fvi}(t))$ and $F_{xrvi}(\lambda_{rvi}(t))$ represent the longitudinal forces at the front and rear tyre–road interface, respectively, and $\lambda_{fvi}(t)$ and $\lambda_{rvi}(t)$ represent the longitudinal slip ratios of front and rear wheels, respectively. They are calculated as

$$\begin{aligned} \lambda_{fvi}(t) &= \frac{v_i(t) - r_i\ \omega_{fvi}(t)}{v_i(t)} \\ \lambda_{rvi}(t) &= \frac{v_i(t) - r_i\ \omega_{rvi}(t)}{v_i(t)} \end{aligned} \tag{3}$$

where r_i is the tyre radius.

The wheel dynamics is given by

$$\begin{aligned} \dot{\omega}_{fvi}(t) &= \frac{1}{I_{fi}} \left(\tau_{fvi}(t) - r_i F_{xfvi}(\lambda_{fvi}(t))\right) \\ \dot{\omega}_{rvi}(t) &= \frac{1}{I_{ri}} (\tau_{rvi}(t) - r_i F_{xrvi}(\lambda_{rvi}(t))) \end{aligned} \tag{4}$$

where $\omega_{fvi}(t)$ and $\omega_{rvi}(t)$ are the angular speeds of front and rear wheels, respectively, I_{fi} and I_{ri} are the moment of inertia of front and rear wheels, respectively, and $\tau_{fvi}(t)$ and $\tau_{rvi}(t)$ are the transmitted torques to the front and rear wheels, respectively.

The longitudinal force components, $F_{xfvi}(\lambda_{fvi}(t))$ and $F_{xrvi}(\lambda_{rvi}(t))$, are computed using the magic formula (MF) tyre model proposed by Pacejka (2005) because the MF tyre model gives a good representation of forces acting on the tyre–road interface for a wide range of operating conditions. The magnitude of the longitudinal force depends on the

longitudinal slip ratios presented by equation (3) and the normal forces at the tyre–road interface. The normal forces at the front and rear tyre–road interface for the i^{th} vehicle are given by

$$\begin{aligned} F_{zfvi}(t) &= \frac{m_{vi} g l_{rvi} \cos(\theta) - F_{avi}(t) h_{ai} - m_{vi} \ddot{x}_i(t) h_{cgi}}{L_i} \\ &\quad - \frac{m_{vi} g h_{cgi} \sin(\theta)}{L_i} \\ F_{zrvi}(t) &= \frac{m_{vi} g l_{fvi} \cos(\theta) + F_{avi}(t) h_{ai} + m_{vi} \ddot{x}_i(t) h_{cgi}}{L_i} \\ &\quad + \frac{m_{vi} g h_{cgi} \sin(\theta)}{L_i} \end{aligned} \tag{5}$$

where $\ddot{x}_i(t)$ is the longitudinal acceleration, h_{cgi} is the height of the centre of gravity (C.G.) of the vehicle, h_{ai} is the height of the location at which the equivalent aerodynamic force acts, θ represents the road inclination l_{fvi} and l_{rvi} are the longitudinal distance of the front axle and rear axle from the C.G. of the vehicle, respectively, and $L_i = l_{fvi} + l_{rvi}$.

Now, using the MF tyre model, the longitudinal forces at front and rear tyre–road interface are calculated as

$$\begin{aligned} F_{xfvi}\left(\lambda_{xfvi}(t)\right) &= D_{xfi} \sin\left(C_{xfi} \tan^{-1}\left(B_{xfi}\lambda_{xfi}(t)\right.\right. \\ &\quad \left.\left. - E_{xfi}\left(B_{xfi}\lambda_{xfi}(t) - \tan^{-1}\left(B_{xfi}\lambda_{xfi}(t)\right)\right)\right)\right) + S_{Vfi} \\ F_{xrvi}(\lambda_{xrvi}(t)) &= D_{xri} \sin\left(C_{xri} \tan^{-1}(B_{xri}\lambda_{xri}(t)\right. \\ &\quad \left. - E_{xri}(B_{xri}\lambda_{xri}(t) - \tan^{-1}(B_{xri}\lambda_{xri}(t)))\right) + S_{Vri} \end{aligned} \tag{6}$$

where $\lambda_{xfvi}(t) = \lambda_{fvi}(t) + S_{Hfi}$ and $\lambda_{xrvi}(t) = \lambda_{rvi}(t) + S_{Hri}$.

The MF model parameters, $B_{xf/ri}$, $C_{xf/ri}$, $D_{xf/ri}$, $E_{xf/ri}$, $S_{Hf/ri}$ and $S_{Vf/ri}$, corresponding to front and rear tyre–road interface, were obtained from the vehicle dynamic simulation software, IPG TruckMaker® (IPG Automotive, IPG, 2018).

Now, $F_{Ri}(t)$ in equation (2) can be expressed as

$$\begin{aligned} F_{Rvi}(t) &= F_{avi}(t) + R_{xfvi}(t) + R_{xrvi}(t) + F_{\text{grad}}(t) \\ &= \rho\ a_{fi}\ C_{Di}(t)\left(\frac{v_i(t)^2}{2}\right) + f\left(F_{zfvi}(t) + F_{zrvi}(t)\right) \\ &\quad + m_{vi} g \sin(\theta) \end{aligned} \tag{7}$$

where $F_{avi}(t)$ represents the force due to aerodynamic drag, R_{xfvi} and R_{xrvi} are the forces due to rolling resistance at the front and rear wheels, respectively, and F_{grad} represents the force component due to the road slope. The aerodynamic drag force is given by $F_{avi}(t) = \rho\ a_{fi} C_{Di}(t)(v_i(t)^2/2)$, where ρ is the air density, $C_{Di}(t)$ represents the aerodynamic drag coefficient and a_{fi} represents the vehicle frontal area. In this work, the drag coefficient $C_{Di}(t)$ is represented as a function of inter-vehicular distance between two individual vehicles in the platoon as $C_{Di}(t) = C_{Di0}(c_1 d_i(t)^{c_2} + c_3)$ (Hussein and Rakha 2020), where C_{Di0} represents the individual vehicle drag coefficient (if not operating in a platoon formation), $d_i(t)$ represents the inter-vehicular distance between two vehicles and c_1, c_2, and c_3 are constants obtained empirically. The rolling resistance is characterised by the rolling resistance coefficient, f, and the normal forces at both front and rear tyre–road interface, $F_{zfvi}(t)$ and $F_{zrvi}(t)$, respectively.

3. Electric motor and pneumatic actuator models for electric HCRV

In an EV, the drive/propulsion torque is provided by the electric motor, and typically, most of the HCRVs are rear wheel driven. In EVs, an induction motor is widely used as the actuation mechanism (Ehsani et al., 2018). The transfer function representation of the motor model is given by

$$P_m(s) = m_a \frac{V_{dc}}{2} e^{(-T_{dm}/2)s} \frac{K_m}{1 + \tau_m s} \tag{8}$$

where m_a is the modulation index of the inverter circuit, $V_{dc}/2$ is the inverter gain, T_{dm} is the PWM delay and K_m and τ_m represent the gain and time constant of the electric motor, respectively. A detailed derivation of this transfer function is presented in Subramaniyam and Subramanian (2019). During braking, EVs use regenerative braking strategy, which would in turn improve the energy efficiency (Lv et al., 2015), and the same motor model described by equation (8) has been used in this study to characterise the same.

Practically, during braking, the required brake force demand would be higher than that of provided by the regenerative braking force. To address this issue, the conventional friction brake system coexists with the regenerative brake system. In HCRVs, pneumatic brakes are the commonly used friction brake system, which uses compressed air as the actuation medium. Pneumatic brake system is known to have significant time delay due to factors such as compressibility of air, pipe lengths and valve response time. There is also a delay in the pressure build up in the brake actuator. While modelling brake response, it is common to include these factors as the time delay (T_d) and the time constant (τ_d). Sridhar et al. (2017) conducted hardware-in-loop experiments and characterised the air brake system using a first-order process with time delay transfer function given by

$$P(s) = \frac{1}{1 + \tau_d s} e^{-T_d s} \tag{9}$$

In this study, equation (9) was used to model the friction brake system dynamics. The specific values for time constant (τ_d) and time delay (T_d) have also been experimentally obtained as τ_d = 260 ms and T_d = 45 ms, respectively (Sridhar et al., 2017), and these values have been utilised in this study.

3.1. Cooperative braking control strategy

In EVs, it is imperative to use both friction and regenerative braking in a cooperative manner to achieve optimum braking performance. Usually, regenerative braking is applied only on the driven wheels (rear wheels for the class of vehicles considered in this study), and friction braking on front and rear wheels. For the ith vehicle in the platoon, this can be represented as

$$\begin{aligned} F_{bfi} &= F_{bfi_{\text{fric}}} \\ F_{bri} &= F_{bri_{\text{fric}}} + F_{bri_{\text{regen}}} \end{aligned} \tag{10}$$

where F_{bfi} and F_{bri} represent the front and rear wheel braking forces, respectively, $F_{bfi_{\text{fric}}}$ and $F_{bri_{\text{fric}}}$ represent the friction brake force components of front and rear wheels, respectively, and $F_{bri_{\text{regen}}}$ represents the regenerative braking force applied at the rear wheels.

The two commonly used cooperative braking strategies are the series cooperative braking (SCB) strategy and the parallel cooperative braking (PCB) strategy (Ehsani et al., 2018). In SCB, during the initial phase of braking, if the braking force demand is less than the maximum available regenerative braking force, then the regenerative braking is applied first. When the desired braking force is more than the maximum regenerative braking force, friction braking is applied on both front and rear wheels.

In PCB, both regenerative (on driven wheels) and friction braking forces (on both front and rear wheels) are applied simultaneously, and the regenerative braking force is applied as a fraction of the total braking force (F_b). This can be represented as

$$F_{bri_{\text{regen}}} = \gamma\, F_b \tag{11}$$

where γ is the ratio of regenerative braking force to the total braking force. Also, the distribution between front and rear braking forces follow a linear proportion, such that

$$\frac{F_{bfi}}{F_{bri}} = \frac{\beta}{1-\beta} \tag{12}$$

where F_{bfi} and F_{bri} are the front and rear brake forces, respectively, and $0 < \beta < 1$. Because maintaining stability is of prime concern during the string stable controller design, a cooperative braking strategy using PCB has been adopted in this study, so that the brake force can be appropriately distributed between driven and non-driven wheels.

4. Impact of battery position on vehicle dynamics

The battery placement has a direct impact on the HCRV performance and ride comfort (Suriyamoorthy et al., 2019). With respect to different battery placement locations, the longitudinal and vertical C.G. locations vary and this would directly affect the vehicle dynamics considerably.

For this analysis, the battery pack was lumped together as a single mass as

$$m_{bat} = N_s N_p m_{cell} \tag{13}$$

where m_{bat} is the total mass of the battery pack, N_s and N_p represent the number of cells in series and parallel, respectively, and m_{cell} indicates the mass of each individual cell.

If l_{fbi} represents the longitudinal C.G. position of battery from the front axle and h_{bi} represents the vertical C.G. height of battery for an ith vehicle, then the longitudinal C.G. position of the EV (l_{fvi}) is given by

$$l_{fvi} = \frac{m_i l_{fi} + m_{bat} l_{fbi}}{m_{vi}} \tag{14}$$

where $m_i = m_{vi} - m_{bat}$, and l_{fi} represents the longitudinal C.G. position of the vehicle from the front axle without the battery pack. Similarly, the vertical C.G. position of the EV (h_{cgvi}) can be presented as

$$h_{cgvi} = \frac{m_i h_{cgi} + m_{bat} h_{bi}}{m_{vi}} \tag{15}$$

The change in C.G. would affect the vehicle dynamics (equations (1) and (2)) directly through the front and rear normal forces, presented by equation (5). For the C.G. locations presented in equations (14) and (15), the normal force equations can be represented as

$$\begin{aligned} F_{zfvi}(t) &= \frac{m_{vi} g l_{rvi} \cos(\theta) - F_{ai}(t) h_{ai} - m_{vi} \ddot{x}_i(t) h_{cgvi}}{L_i} \\ &\quad - \frac{m_{vi} g h_{cgvi} \sin(\theta)}{L_i} \\ F_{zrvi}(t) &= \frac{m_{vi} g l_{fvi} \cos(\theta) + F_{ai}(t) h_{ai} + m_{vi} \ddot{x}_i(t) h_{cgvi}}{L_i} \\ &\quad + \frac{m_{vi} g h_{cgvi} \sin(\theta)}{L_i} \end{aligned} \tag{16}$$

Now, assuming $h_{ai} = h_{cgvi}$ and substituting $m_{vi} = m_i + m_{bat}$ and equations (14) and (15) gives

$$\begin{aligned} F_{zfvi}(t) = &\frac{(m_i + m_{bat}) g l_{rvi} \cos(\theta) - F_{ai}(t) \left(\frac{m_i h_{cgi} + m_{bat} h_{bi}}{(m_i + m_{bat})} \right)}{L_i} \\ &- \frac{(m_i + m_{bat}) \ddot{x}_i(t) \left(\frac{m_i h_{cgi} + m_{bat} h_{bi}}{(m_i + m_{bat})} \right)}{L_i} \\ &- \frac{(m_i + m_{bat}) g \left(\frac{m_i h_{cgi} + m_{bat} h_{bi}}{(m_i + m_{bat})} \right) \sin(\theta)}{L_i} \end{aligned}$$

$$F_{zrvi}(t) = \frac{(m_i + m_{bat})g\left(\frac{m_i l_{fi} + m_{bat} l_{fbi}}{(m_i + m_{bat})}\right)\cos(\theta)}{L_i} + \frac{F_{ai}(t)\left(\frac{m_i h_{cgi} + m_{bat} h_{bi}}{(m_i + m_{bat})}\right)}{L_i} + \frac{(m_i + m_{bat})\ddot{x}_i(t)\left(\frac{m_i h_{cgi} + m_{bat} h_{bi}}{(m_i + m_{bat})}\right)}{L_i} + \frac{(m_i + m_{bat})g\left(\frac{m_i h_{cgi} + m_{bat} h_{bi}}{(m_i + m_{bat})}\right)\sin(\theta)}{L_i} \quad (17)$$

On rearranging

$$F_{zfvi}(t) = \frac{m_i g l_{rvi}\cos(\theta) - \frac{m_i F_{ai}(t) h_{cgi}}{m_i + m_{bat}} - m_i \ddot{x}_i(t) h_{cgi}}{L_i} - \frac{m_i g h_{cgi}\sin(\theta)}{L_i} + \frac{m_{bat} g l_{rvi}\cos(\theta)}{L_i} - \frac{\frac{m_{bat} F_{ai}(t) h_{bi}}{(m_i + m_{bat})}}{L_i} - \frac{m_{bat}\ddot{x}_i(t) h_{bi}}{L_i} - \frac{m_{bat} g h_{bi}\sin(\theta)}{L_i}$$

$$F_{zrfvi}(t) = \frac{m_i g l_{fi}\cos(\theta) + \frac{m_i F_{ai}(t) h_{ai}}{m_i + m_{bat}} + m_i \ddot{x}_i(t) h_{cgi}}{L_i} + \frac{m_i g h_{cgi}\sin(\theta)}{L_i} + \frac{m_{bat} g l_{fbi}\cos(\theta)}{L_i} + \frac{\frac{m_{bat} F_{ai}(t) h_{bi}}{(m_i + m_{bat})}}{L_i} + \frac{m_{bat}\ddot{x}_i(t) h_{bi}}{L_i} + \frac{m_{bat} g h_{bi}\sin(\theta)}{L_i} \quad (18)$$

From equation (18), it can be understood that the variation of l_{fbi} and h_{bi} has direct impact on the normal forces generated at the tyre–road interface and hence on the longitudinal traction/brake forces.

In this regard, different locations for battery placement were considered and their effects on vehicle dynamics; and hence, string stability was analysed in this study. Figure 2 presents three different battery locations, front (F), middle (M) and rear (R), used for the analysis. The lumped battery pack has been placed at each of these locations, corresponding to $l_{fbi} = 0$, $l_{fbi} = L_i/2$ and $l_{fbi} = L_i$, respectively. The hub motor (M_r) placement in the rear drive configuration is also presented. Also, it was assumed that the variation in battery configuration does not affect the C.G. height of the vehicle (h_{cgvi}). This assumption is valid because the battery pack is constrained to move only in the longitudinal direction (as shown in Figure 2) and is maintained at a constant height from the ground.

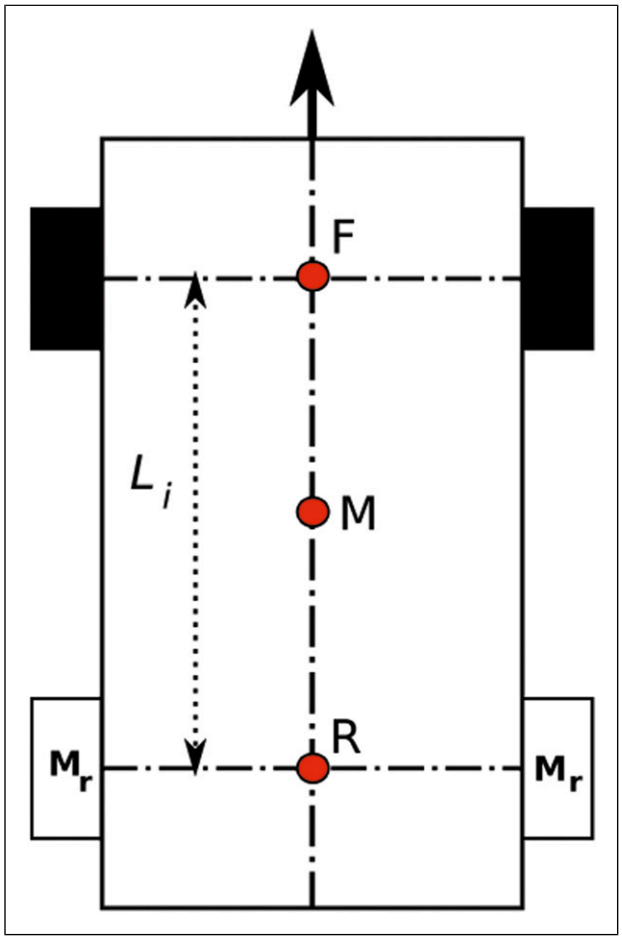

Figure 2. C.G. location variation for both laden and unladen electric HCRV for different battery locations. Note: C.G.: center of gravity; HCRV: heavy commercial road vehicle.

Table 1 presents the effect of placing the battery pack at different locations as indicated in Figure 2. Different cases were analysed for both laden and unladen electric HCRVs. For each condition presented in Table 1, longitudinal C.G. position l_{fvi} was calculated using equation (14) and has been used to analyse the effects of change in battery position on the normal force distribution. The variation in the front and rear normal forces with respect to change in C.G. location is also presented in Table 1.

5. String stable controller design

As shown in Figure 1, the platoon consists of $N+1$ vehicles, with one leader and N followers. The longitudinal motion of the leader vehicle is characterised by

$$\dot{x}_0(t) = v_0(t) \quad (19)$$

where $x_0(t)$ and $v_0(t)$ are the position and longitudinal speed of the leader vehicle, respectively. From equations (1) and

Table 1. Effects of different battery placement locations on C.G. variation and normal load distribution.

Load	Battery position (m)	l_{fvi} (m)	C.G. location (m)	$F_{zfvi}(t)$ (N)	$F_{zfvi}(t)$ (N)
Laden	$l_{fbi} = 0$	$l_{fvi} = (m_i/m_{vi})l_{fi}$	$l_{fvi} < l_{fi}$ $l_{rvi} > l_{ri}$	↑	↓
	$l_{fbi} = L_i/2$	$l_{fvi} = (m_i/m_{vi})l_{fi} + (m_{bat}/m_{vi})(L_i/2)$	$l_{fvi} \approx l_{fi}$ $l_{rvi} \approx l_{ri}$	↔	↔
	$l_{fbi} = L_i$	$l_{fvi} = (m_i/m_{vi})l_{fi} + (m_{bat}/m_{vi})L_i$	$l_{fvi} > l_{fi}$ $l_{rvi} < l_{ri}$	↓	↑
Unladen	$l_{fbi} = 0$	$l_{fvi} = (m_i/m_{vi})(L_i/2)$	$l_{fvi} < l_{fi}$ $l_{rvi} > l_{ri}$	↑	↓
	$l_{fbi} = L_i/2$	$l_{fvi} = L_i/2$	$l_{fvi} = l_{fi}$ $l_{rvi} = l_{ri}$	↔	↔
	$l_{fbi} = L_i$	$l_{fvi} = (m_i + 2m_{bat}/2m_{vi})L_i$	$l_{fvi} > l_{fi}$ $l_{rvi} < l_{ri}$	↓	↑

↑: increase; ↔: no/minor change; ↓: decrease.
Note: C.G.: centre of gravity.

(2), the longitudinal motion of the follower vehicles is described by

$$\begin{aligned} \dot{x}_i(t) &= v_i(t) \\ \dot{v}_i(t) &= \frac{1}{m_{vi}}\left(F_{xfvi}(\lambda_{fi}(t)) + F_{xrvi}(\lambda_{ri}(t)) - F_{Rvi}(t)\right) \end{aligned} \tag{20}$$

where $i = 1 \ldots N$. On substituting $F_{xfvi}(\lambda_{fvi}(t))$ and $F_{xrvi}(\lambda_{rvi}(t))$ from equations (4) in (20), one can obtain the follower vehicle dynamics as

$$\begin{aligned} \dot{v}_i(t) = \frac{1}{m_{vi}}\Bigg[&\frac{1}{r_i}\left(\tau_{fvi}(t) - I_{fi}\dot{\omega}_{fvi}(t)\right) \\ &+ \frac{1}{r_i}\left(\tau_{rvi}(t) - I_{ri}\dot{\omega}_{rvi}(t)\right) - F_{Rvi}(t)\Bigg] \end{aligned} \tag{21}$$

5.1. Control objective

For the vehicular platoon, the spacing between a pair of vehicles is given by

$$d_i(t) = x_{i-1}(t) - x_i(t) \tag{22}$$

and the desired inter-vehicular distance is defined as

$$s_d(t) = s_o + h_i v_i(t) \tag{23}$$

where s_o and h_i represent standstill spacing and the constant time headway (CTH), respectively. Now, the spacing error between two consecutive vehicles can be written as

$$e_i(t) = d_i(t) - s_d(t) \tag{24}$$

The control objective here is to drive the spacing error between consecutive vehicles to zero, such that

$$d_i(t) \to s_o + h_i v_i(t) \tag{25}$$

5.2. Sliding Mode Controller design

In this study, the following sliding function has been defined for the design of SMC–based control action (Guo et al., 2016)

$$s_i(t) = e_i(t) + \int_0^t \kappa e_i(\tau)d\tau \tag{26}$$

Here, $e(t)$ is the inter-vehicular spacing error given by equation (24). The term κ is a positive constant, which defines the slope of the sliding function. In this study, a sliding function with an integral term is selected here to avoid the use of derivative of acceleration (jerk) data from preceding vehicles. If one were to use the standard sliding function, $s_i(t) = \dot{e}_i(t) + \kappa e_i(t)$, then the jerk terms would appear while obtaining the control equation by taking the first derivative of the sliding function. This additional data requirement would make the controller design complex and subsequently makes controller implementation difficult. The above sliding function given by equation (26) has been defined for driving the inter-vehicular spacing error between two consecutive vehicles to zero. However, for string stability, the sliding function should be redefined for attenuating the spacing error propagation (Guo et al., 2016). For this, the sliding function is redefined as

$$S_i(t) = \begin{cases} qs_i(t) - s_{i+1}(t), & i = 1,\ldots,N-1 \\ qs_i(t), & i = N \end{cases} \tag{27}$$

where $q > 0$.

For designing SMC control equation, PRERL structure has been used in this work (Devika and Thomas 2017) that is given by

$$\dot{S}_i(t) = -\frac{\psi}{\delta_0 + (1-\delta_0)e^{-\alpha|S_i(t)|^p}}|S_i(t)|^\chi \text{sign}(S_i(t)) \tag{28}$$

Here, $\psi > 0$ is the controller gain, and $\delta_0 < 1$, $\alpha > 0$, $0 < \chi < 0.5$ and $p > 0$ are controller parameters that affect the reaching time and chattering mitigation properties, respectively. The above structure is defined in such a way that at the starting of the reaching phase (i.e. when sliding function takes larger magnitudes), the overall controller gain is increased as discussed below:

When $S_i(t) \to \infty$, the denominator term in PRERL structure $\delta_0 + (1-\delta_0)e^{-\alpha|S_i(t)|^p} \to \delta_0$ and the overall controller gain becomes ψ/δ_0.

Now, towards the sliding surface (i.e. when sliding function approaches zero), when $S_i(t) \to 0$, the denominator term in PRERL structure $\delta_0 + (1-\delta_0)e^{-\alpha|S_i(t)|^p} \to 1$ and the overall controller gain becomes ψ.

Because $\delta_0 < 1$, the controller gain at the initial phase of transient operation is greater than its value near the sliding surface, that is, $(\psi/\delta_0) > \psi$ for any chosen ψ. Hence, because of the higher control action in the initial phase, reaching time is reduced (reaching speed is increased) and due to the smaller control action near the sliding surface, chattering is reduced (by limiting over actuation near the vicinity of sliding surface). Along with this adaptive variation of controller gain, the selection of the power rate term, χ in the range $0 < \chi < 0.5$, further reduces chattering. The above explained phenomena have been discussed in detail in Devika and Thomas (2017) and proofs for these claims have been presented in Devika and Thomas (2017).

It is to be noted that in PRERL, the 'sign' function is present. Hence, complete chattering elimination is not possible. However, in PRERL, through the adaptive gain variation in the reaching phase and through the selection of the suitable power rate term (χ), chattering can be attenuated to the extent of obtaining smooth control action (Devika and Thomas, 2017). In addition to chattering attenuation property, PRERL also possesses advantages such as fast closed loop response, ability to satisfy control constraints and robustness, which would further enhance the performance of the proposed string stable controller (Devika and Thomas, 2017).

Brake Mode: During braking, the proportion of the brake torque applied on the front and rear wheels follow a linear proportion, β, such that

$$\frac{\tau_{fvi}(t)}{\tau_{rvi}(t)} = \frac{\beta}{1-\beta} \tag{29}$$

On using this linear proportion in equation (21)

$$\begin{aligned}\dot{v}_i(t) = \frac{1}{m_{vi}}\Bigg[&\frac{1}{r_i}\left(\frac{\beta}{1-\beta}\tau_{rvi}(t) - I_{fi}\dot{\omega}_{fvi}(t)\right)\\ &+\frac{1}{r_i}\left(\tau_{rvi}(t) - I_{ri}\dot{\omega}_{rvi}(t)\right) - F_{Rvi}(t)\Bigg]\end{aligned} \tag{30}$$

On rearranging the above equation

$$\begin{aligned}\dot{v}_i(t) = \tau_{rvi}(t)&\left[\frac{1}{m_{vi}r_i}\left(1+\frac{\beta}{1-\beta}\right)\right]\\ &-\frac{1}{m_{vi}r_i}\left(I_{fi}\dot{\omega}_{fvi}(t) + I_{ri}\dot{\omega}_{rvi}(t)\right) - \frac{F_{Rvi}(t)}{m_{vi}}\end{aligned} \tag{31}$$

Here, τ_{rvi} is the control input ($u_i(t)$) which needs to be synthesised using SMC. On evaluating the first derivatives of equations (27) and (26), and using the vehicle dynamics equation given by equation (31) and the PRERL structure given by equation (28), one can write

$$\begin{aligned}\dot{S}_i(t) &= q(v_{i-1}(t) - v_i(t)) + q\kappa e_i(t) - \dot{e}_{i+1}(t) - \kappa e_{i+1}(t)\\ &\quad - qh_i\left[\frac{-1}{m_{vi}r_i}\left(I_{fi}\dot{\omega}_{fvi}(t) + I_{ri}\dot{\omega}_{rvi}(t)\right)\right.\\ &\quad \left. - \frac{F_{Rvi}(t)}{m_{vi}}\right] - qh_i\left[\frac{1}{m_{vi}r_i}\left(1+\frac{\beta}{1-\beta}\right)\right]u_i(t)\\ &= -\frac{\psi}{\delta_0 + (1-\delta_0)e^{-\alpha|S_i(t)|^p}}|S_i(t)|^{\chi}\mathrm{sign}(S_i(t))\\ i &= 1,\ldots,N-1\end{aligned}$$

$$\begin{aligned}\dot{S}_N(t) &= q(v_{N-1}(t) - v_N(t)) + q\kappa e_N(t)\\ &\quad - qh_N\left[\frac{-1}{m_{vN}r_N}\left(I_{fN}\dot{\omega}_{fvN}(t) + I_{rN}\dot{\omega}_{rvN}(t)\right)\right.\\ &\quad \left. - \frac{F_{RvN}(t)}{m_{vN}}\right] - qh_N\left[\frac{1}{m_{vN}r_N}\left(1+\frac{\beta}{1-\beta}\right)\right]u_N(t)\\ &= -\frac{\psi}{\delta_0 + (1-\delta_0)e^{-\alpha|S_N(t)|^p}}|S_N(t)|^{\chi}\mathrm{sign}(S_N(t))\end{aligned} \tag{32}$$

From the above expressions, the torque control input $u_i(t) = \tau_{rvi}(t)$ can be obtained as

$$\begin{aligned}\tau_{rvi}(t) = &\frac{-1}{qh_i\left[\frac{1}{m_{vi}r_i}\left(1+\frac{\beta}{1-\beta}\right)\right]}\\ &\times\left[\frac{-\psi}{\delta_0 + (1-\delta_0)e^{-\alpha|S_i(t)|^p}}|S_i(t)|^{\chi}\mathrm{sign}(S_i(t))\right.\\ &- q(v_{i-1}(t) - v_i(t)) - q\kappa e_i(t) + \dot{e}_{i+1}(t) + \kappa e_{i+1}(t)\\ &\left. + qh_i\left[\frac{-1}{m_{vi}r_i}\left(I_{fi}\dot{\omega}_{fvi}(t) + I_{ri}\dot{\omega}_{rvi}(t)\right) - \frac{F_{Rvi}(t)}{m_{vi}}\right]\right]\\ &i = 1,\ldots,N-1\end{aligned} \tag{33}$$

and for the last vehicle in the platoon

$$\tau_{rvN}(t) = \frac{-1}{qh_N\left[\frac{1}{m_{vN}r_N}\left(1+\frac{\beta}{1-\beta}\right)\right]} \times \left[\frac{-\psi}{\delta_0+(1-\delta_0)e^{-\alpha|S_N(t)|^p}}|S_N(t)|^{\chi}\text{sign}(S_N(t)) - q(v_{N-1}(t)-v_N(t)) - q\kappa e_N(t) + qh_N\left[\frac{-1}{m_{vN}r_i}\left(I_{fN}\dot{\omega}_{fvN}(t)+I_{rN}\dot{\omega}_{rvN}(t)\right)-\frac{F_{RvN}(t)}{m_{vN}}\right]\right] \quad (34)$$

Now, using (29), the torque inputs for the front wheels can be obtained as

$$\tau_{fvi}(t) = \frac{\beta}{1-\beta}\tau_{rvi}(t) \quad i = 1,\ldots,N-1 \quad (35)$$

and for the last vehicle in the platoon

$$\tau_{fvN}(t) = \frac{\beta}{1-\beta}\tau_{vrN}(t) \quad (36)$$

For the rear wheel–driven EV, by using PCB strategy, the regenerative braking torque is applied as a fraction of the rear wheel torque input $\tau_{rvi}(t)$. Applying this, the regenerative brake input $\tau_{rvi_{\text{regen}}}(t)$ can be calculated as

$$\tau_{rvi_{\text{regen}}}(t) = \gamma\ \tau_{rvi}(t) \quad (37)$$

and for the last vehicle in the platoon

$$\tau_{rvN_{\text{regen}}}(t) = \gamma\ \tau_{rvN}(t) \quad (38)$$

Drive Mode: In a rear wheel–driven EV, during drive mode, $\tau_{fvi}(t) = 0$, $\tau_{rvi}(t) = \tau_{vi}(t)$, which would be provided by the electric motor. Now, in equation (21), substituting $\tau_{fvi}(t) = 0$ and following the same controller design steps as presented above, the drive torque inputs can be obtained as

$$\tau_{vi}(t) = \frac{-m_{vi}r_i}{qh_i}\left[\frac{-\psi}{\delta_0+(1-\delta_0)e^{-\alpha|S_i(t)|^p}}|S_i(t)|^{\chi}\text{sign}(S_i(t)) - q(v_{i-1}(t)-v_i(t)) - q\kappa e_i(t) + \dot{e}_{i+1}(t) + \kappa e_{i+1}(t) + qh_i\left[\frac{-1}{m_{vi}r_i}\left(I_{fi}\dot{\omega}_{fvi}(t)+I_{ri}\dot{\omega}_{rvi}(t)\right)-\frac{F_{Rvi}(t)}{m_{vi}}\right]\right] \quad i = 1,\ldots,N-1 \quad (39)$$

and for the last vehicle in the platoon

$$\tau_{vN}(t) = \frac{-m_{vN}r_N}{qh_N}\left[\frac{-\psi}{\delta_0+(1-\delta_0)e^{-\alpha|S_N(t)|^p}}|S_N(t)|^{\chi}\text{sign}(S_N(t)) - q(v_{N-1}(t)-v_N(t)) - q\kappa e_N(t) + qh_N\left[\frac{-1}{m_{vN}r_i}\left(I_{fN}\dot{\omega}_{fvN}(t)+I_{rN}\dot{\omega}_{rvN}(t)\right)-\frac{F_{RvN}(t)}{m_{vN}}\right]\right] \quad (40)$$

5.3. String stability analysis

The vehicle platoon is said to be string stable if the inter-vehicular spacing errors between consecutive vehicles are bounded uniformly in time, provided the initial spacing errors are bounded (Swaroop, 1997). To ensure strong string stability, the spacing errors should not get amplified along the platoon (Guo et al., 2016). According to previous related studies (Guo et al., 2016; Kwon and Chwa, 2014), the platoon is string stable in the strong sense, if the error propagation transfer function given by

$$G_i(s) = \frac{E_{i+1}(s)}{E_i(s)} \quad (41)$$

follows the condition

$$|G_i(s)| \le 1 \quad \forall i = 1,\ldots,N \quad (42)$$

Here, $E_i(s)$ and $E_{i+1}(s)$ denote the Laplace transform of spacing error propagation between consecutive pairs of vehicles in the platoon. Because $S_i(t) = qs_i(t) - s_{i+1}(t)$ converges to zero in a finite time, based on (27), one can write

$$qs_i(t) = s_{i+1}(t) \quad (43)$$

Now, using (26)

$$q\left(e_i(t) + \int_0^t \kappa e_i(\tau)d\tau\right) = e_{i+1}(t) + \int_0^t \kappa e_{i+1}(\tau)d\tau \quad (44)$$

On taking Laplace transform on both sides

$$q\left[E_i(s) + \frac{\kappa}{s}E_i(s)\right] = E_{i+1}(s) + \frac{\kappa}{s}E_{i+1}(s) \quad (45)$$

which gives the spacing error propagation transfer function as

$$G_i(s) = \frac{E_{i+1}(s)}{E_i(s)} = q \quad (46)$$

For ensuring strong string stability, $|G_i(s)| \le 1$, and hence, by selecting the parameter q in the range $0 < q \le 1$, the presented controller design framework would ensure strong string stable platoon operation. To ensure error attenuation along the length of the platoon, in this work, the value of q is chosen to be 0.9.

6. Results and discussions

The performance evaluation of the string stability controller and the effect of battery placement on different locations have been presented through numerical simulations. To simulate the longitudinal dynamics and operations of an electric HCRV platoon under different operating scenarios, a complete vehicle dynamics platoon model consisting of

Table 2. Vehicle and actuation system parameters (Suriyamoorthy et al., 2019; Subramaniyam and Subramanian 2019; Sridhar et al., 2017).

Parameter	Value	Parameter	Value
Vehicle parameters		Battery parameters	
Vehicle fully laden mass	16200 kg	Number of battery cells in series	162
Vehicle fully unladen mass	4700 kg	Number of battery cells in parallel	157
Wheel radius	0.53 m	Mass of each battery cell	48 g
Front axle distance from C.G (laden)	3.4 m	Actuation parameters	
Rear axle distance from C.G (laden)	2 m	Friction brake system time delay	45 ms
Front axle distance from C.G (unladen)	2.7 m	Friction brake system time constant	260 ms
Rear axle distance from C.G (unladen)	2.7 m	Modulation index	0.9176
C.G height (laden)	1.3 m	Inverter gain	400
C.G height (unladen)	1 m	PWM delay	0.1 ms
Frontal area	8.91 m^2	Electric motor gain	218.7
Density of the air	1.177 kg/m^3	Electric motor time constant	0.05498
Moment of inertia of front wheels	10 kgm^2		
Moment of inertia of rear wheels	20 kgm^2		

Note: C.G.: centre of gravity.

wheel dynamics, resistive forces, nonlinear MF tyre model and actuation dynamics have been programmed in MATLAB SIMULINK®. The vehicle and actuation system parameters used in this study are presented in Table 2. The detailed test matrix used for the analysis is presented in Figure 3. Operations of both laden and unladen platoons on dry road ($\mu = 0.8$) and wet road ($\mu = 0.5$) conditions were considered. A platoon of seven electric HCRVs (6 follower vehicles and one leader) was considered in this study. Electric vehicle platoon operation on a level road ($\theta = 0$), uphill ($\theta > 0$) and downhill ($\theta < 0$) conditions were analysed for different battery locations and speed profiles. The lumped battery pack was assumed to be placed on three distinct locations, on the front axle, middle and the rear axle locations, indicated as F, M and R in Figure 3. Two different speed profiles, a constant speed profile of 50 km/h and a profile with a speed perturbation were used for the analysis. The complete performance evaluation under different operating conditions and battery locations is presented in Table 3.

Figure 4 illustrates the variation in C.G. locations of the electric HCRV for different battery positions. For the HCRV model considered in this work, for an unladen HCRV, $l_{fi} = l_{ri} = 2.7$ m, and for $l_{fb} = 0$ m, $l_{fvi} = 2.24$ m, and $l_{rvi} = 3.16$ m, indicating increased load at front wheel, as presented in Figure 4. For a laden HCRV, $l_{fi} = 3.4$ m and $l_{ri} = 2.0$ m, and if the battery is placed at F, $l_{fvi} = 3.2$ m, and $l_{rvi} = 2.2$ m, again suggesting an increase in load at the front wheels. As presented in Figure 4, for $l_{fbi} = L_i$, indicating a battery placement at rear axle (R), for the laden scenario, the new C.G locations are found to be $l_{fvi} = 3.55$ m and $l_{rvi} = 1.85$ m, and $l_{fvi} = 3.16$ m and $l_{rvi} = 2.24$ m, for an unladen electric

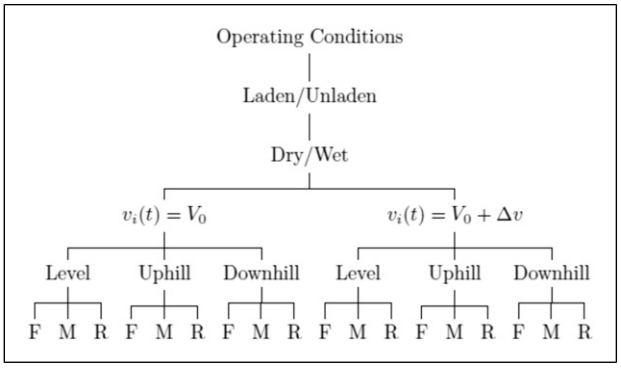

Figure 3. Test matrix.

HCRV. For $l_{fbi} = L_i/2$, for unladen electric HCRV, $l_{fvi} = L_i/2 = l_{fi} = 2.7$ m, and $l_{rvi} = L_i - l_{fvi}/2 = 2.7$ m. Even for a laden electric HCRV, the new C.G. location was found to be much closer to l_{fi} and l_{ri} values at $l_{fvi} = 3.38$ m and $l_{rvi} = 2.02$ m.

To illustrate the advantage of the proposed dynamics-based string stable controller over kinematic–based controllers, a comparative study between kinematic model–based and dynamics model–based string stable controller is presented here. A string stable controller has been designed using the kinematic model of the vehicle and this controller has been tested for string stability. The kinematic model–based controller has also been designed using the PRERL–based SMC strategy. The position of each vehicle in the platoon for the test case – straight and level road, $\mu = 0.8$, $l_{fbi} = L_i/2$ and laden vehicles–using the kinematic–based controller is shown in Figure 5. The same position plot corresponding to the dynamics-based string stable controller (presented in the article) is shown in Figure 6. On comparing these two position

Table 3. Performance evaluation under different operating conditions and battery locations.

Road condition	Loading condition	Battery position	Speed perturbation	String stability
Straight and level road, $\theta = 0$				
Dry	Laden	F/M/R	x	✓/✓/✓
Dry	Laden	F/M/R	✓	✓/✓/✓
Dry	Unladen	F/M/R	x	✓/✓/✓
Dry	Unladen	F/M/R	✓	✓/✓/✓
Wet	Laden	F/M/R	x	✓/✓/✓
Wet	Laden	F/M/R	✓	✓/✓/✓
Wet	Unladen	F/M/R	x	✓/✓/✓
Wet	Unladen	F/M/R	✓	✓/✓/✓
Downhill road condition, $\theta < 0$				
Dry	Laden	F/M/R	x	✓/✓/✓
Dry	Laden	F/M/R	✓	✓/✓/x
Dry	Unladen	F/M/R	x	✓/✓/x
Dry	Unladen	F/M/R	✓	✓/x/x
Wet	Laden	F/M/R	x	✓/x/x
Wet	Laden	F/M/R	✓	x/x/x
Wet	Unladen	F/M/R	x	✓/x/x
Wet	Unladen	F/M/R	✓	x/x/x
Uphill road condition, $\theta > 0$				
Dry	Laden	F/M/R	x	✓/✓/✓
Dry	Laden	F/M/R	✓	x/✓/✓
Dry	Unladen	F/M/R	x	x/✓/✓
Dry	Unladen	F/M/R	✓	x/x/✓
Wet	Laden	F/M/R	x	x/x/✓
Wet	Laden	F/M/R	✓	x/x/✓
Wet	Unladen	F/M/R	x	x/x/✓
Wet	Unladen	F/M/R	✓	x/x/✓

Dry: $\mu = 0.8$, wet: $\mu = 0.5$
Note: F: front axle, M: middle of the wheel base, R: rear axle.

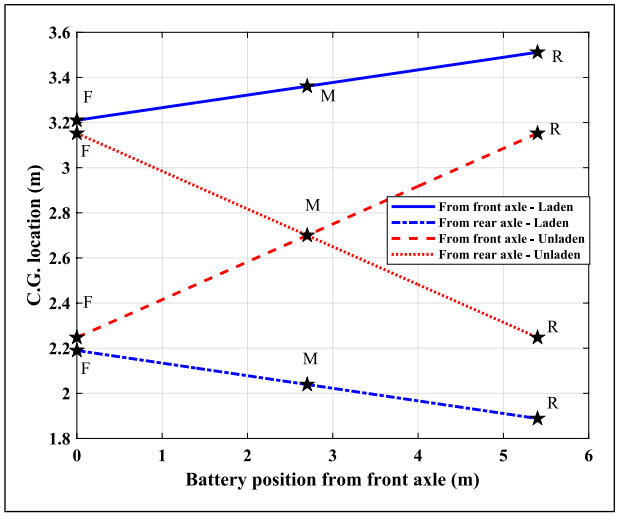

Figure 4. C.G. location variation for both laden and unladen electric HCRV for different battery locations.
Note: C.G.: center of gravity; HCRV: heavy commercial road vehicle.

plots, one can observe that the case where controller was designed using kinematic vehicle model results in collision, whereas the dynamics-based controller avoids collision and maintains string stability. It is to be noted that both the string stable controllers were designed using the same controller parameters. Even re-tuning of the kinematic model–based controller failed to achieve string stability. This comparison shows the advantage of the proposed dynamics-based string stable controllers for HCRV platoons.

Figure 7 presents a sample test case for a laden electric HCRV platoon operating on a straight and level road with a constant longitudinal speed of 50 km/h. A dry road condition is considered with battery pack placed at the middle of the wheel base. Because there was no braking involved, and rear wheel–driven vehicles were used, the front wheel torque input was zero (Figure 7(c)) and the drive torque was provided by the rear mounted electric motor as presented in Figure 7(d).

For an electric HCRV platoon operating on a straight and level road (as shown in Figure 7), the SMC–based string

stable controller was found to be robust enough to accommodate wide range of operating conditions. The change in C.G. because of placing the battery pack at different locations, and having a perturbation in the speed profile, have minimal/no effect on the platoon stability, for both laden and unladen conditions. For different battery placement locations, the C.G. positions varied up to a maximum of 17% and 10% in unladen and laden scenarios (Figure 4), respectively. The designed SMC controller was found to be robust enough to handle these parameter variations and thereby ensuring string stability.

Figure 8 presents a sample set from Table 3 corresponding to $\mu = 0.5$ and a downhill road, laden scenario with the battery pack placed at the front axle location. To simulate downhill road conditions, a road with slope of $-5°$ was considered. For this condition, the controller could ensure string stable operation for the platoon plying with constant speed but was unable to do so for other two battery locations. The downhill road was assumed to be starting at $t = 5$ s and end at $t = 50$ s, and the corresponding speed profile is presented in Figure 8(a). To maintain the speed constant, one has to apply brake continuously for the

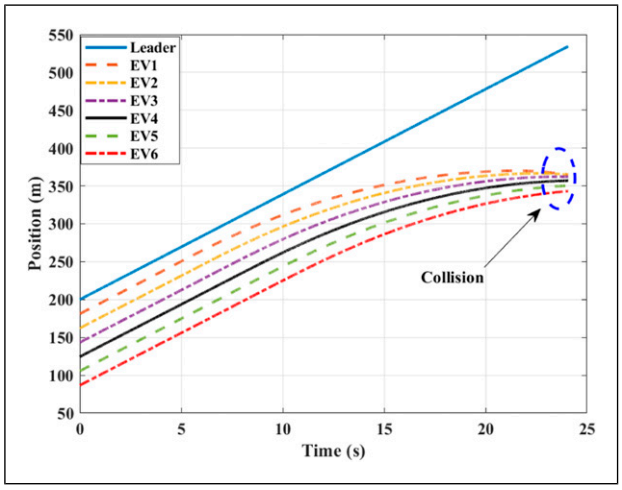

Figure 5. Position profile using the kinematic model–based string stable controller.

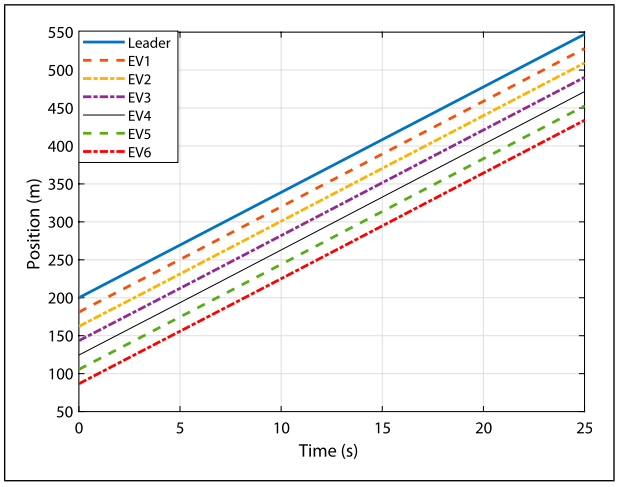

Figure 6. Position profile using the dynamics model–based string stable controller.

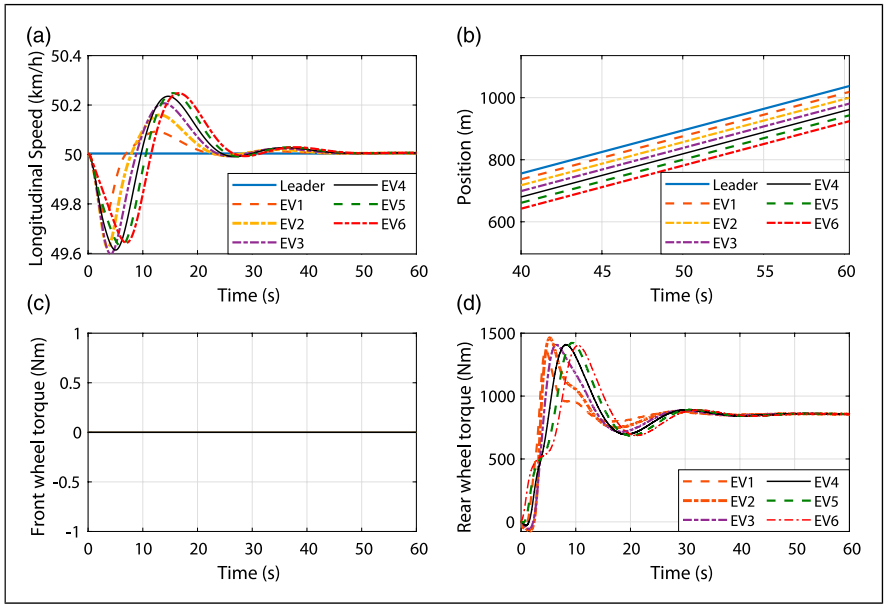

Figure 7. Plots indicating stable platoon operation in a straight and level road, $\mu = 0.8$, $l_{fbi} = L_i/2$ and laden case: (a) longitudinal speed, (b) position, (c) front wheel torque input and (d) rear wheel torque input.

whole duration of traversing the slope. The brake torque generated was split equally between front and rear wheels with $\beta = 0.5$. The front wheel friction torque profile (τ_{fi}) for maintaining constant speed is presented in Figure 8(b). Because PCB strategy was adopted in this article, the torque demand on rear wheels was split between friction braking component (τ_{rfi}) and regenerative braking component (τ_{regen}) with $\gamma = 0.1$, and corresponding profiles are presented in Figures 8(c) and (d). After $t = 50$ s, both front and rear friction torque components would become zero, and the rear motor torque (τ_{mi}) is applied at the rear wheels to maintain the speed.

From the analysis, it was found that the controller could ensure string stability if the platoon was maintaining a constant speed on a dry road surface, irrespective of the battery location. In case of an added perturbation, the rear

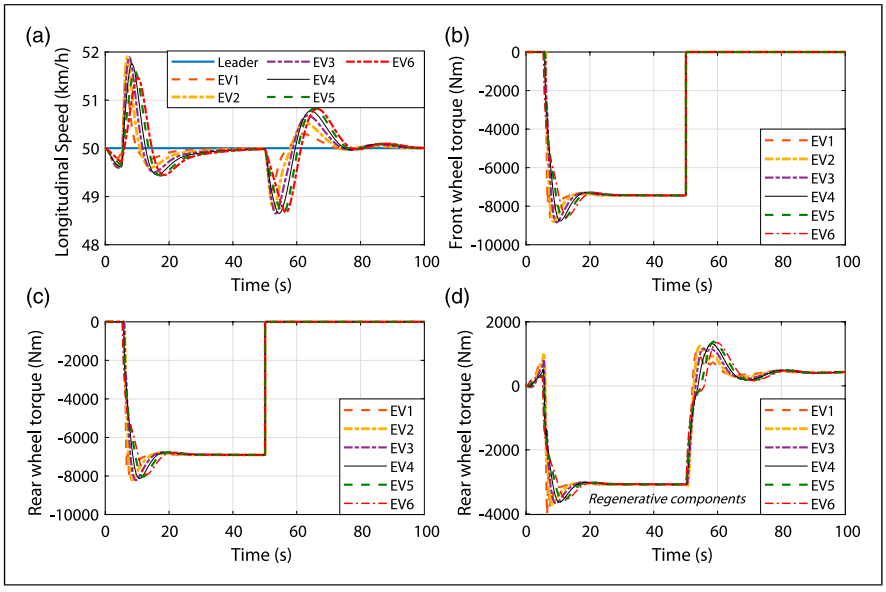

Figure 8. Plots indicating stable platoon operation in a downhill road, $\mu = 0.5$, $l_{fbi} = 0$ and laden case: (a) longitudinal speed, (b) front wheel torque input, (c) rear wheel friction torque input and (d) rear wheel motor torque input (positive value indicates drive torque and negative value indicates braking torque).

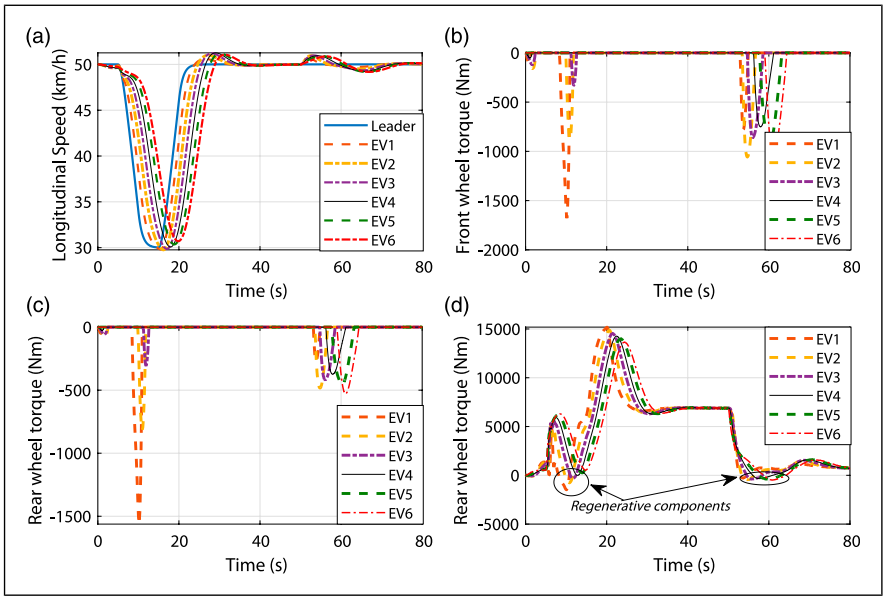

Figure 9. Plots indicating stable platoon operation in a uphill road, $\mu = 0.5$, $l_{fbi} = L$ and laden case: (a) longitudinal speed, (b) front wheel torque input, (c) rear wheel friction torque input and (d) rear wheel motor torque input (positive value indicates drive torque and negative value indicates braking torque).

mounted battery configuration results in collision. In fact, during operation on a downhill road, it is not recommended to place the battery pack at the rear because it would always result in collisions with an exception of the former case (Table 3). This is because of the nature of load distribution during the downhill operation, where it is ideal to have more traction at the front wheels to safely operate the vehicle. Placing the battery pack at the rear axle is counter-intuitive because it would shift the C.G. towards the rear wheels (Figure 4) and decreases the load on front axle. This could affect the braking performance of the HCRVs, which could in turn result in collisions and loss of platoon stability. This could be also inferred from Table 3.

To analyse the effect of battery location on the string stable controller performance, a sample case from Table 3 with $\mu = 0.5$ and $l_{fbi} = L_i$ for a fully laden electric HCRV platoon is presented in Figure 9. A road slope of +5° and a speed perturbation profile with $\Delta v = -20$ km/h (as shown in Figure 9(a)) were considered for the simulations. Being in an uphill travelling scenario, one could expect to achieve the reduction in speed by reducing the drive torque, depending on the perturbation magnitude. For the selected slope and speed perturbation magnitude, initially, the controller attempts to track the perturbation profile by reducing τ_{mi}, but a small amount of braking was needed to reach the speed of 30 km/h. This was shown in the front and rear torque curves (Figures 9(b)–9(d)). The regenerative braking torque component during braking is marked as τ_{regen} in Figure 9(d). Once the desired speed was reached, the rear wheel motor generated enough traction force to accelerate back to the initial speed of 50 km/h. Also, one could notice the steady state torque value needed to maintain the constant speed during the uphill manoeuvre ($\tau_m = 7000$ Nm) is much higher than that of during a level road ($\tau_m = 850$ Nm).

On contrary to the downhill scenario, during uphill operation, placing the battery pack at the rear end of the vehicle ensured a string stable platoon operation irrespective of the road, loading and speed perturbation conditions. The increased load at the rear wheels improves the traction force, and being a rear wheel–driven vehicle, this improves the vehicle stability, and in turn, the platoon stability.

Plots showing spacing error attenuation along the length of the platoon are presented in Figures 10–12, . As one can notice, the spacing error magnitudes are attenuated from vehicle one to vehicle 6. This satisfies the notion of string stability, that is, $|E(i+1)/E(i)| \leq 1$ for all vehicles in the platoon.

It is to be noted that, an SMC–based string stable controller with CTH policy could ensure string stable operation only during non-zero velocity errors, but not during non-zero spacing errors, in the transient phase (Guo et al., 2016). In this article, the string stability performance analysis has been conducted considering zero velocity and

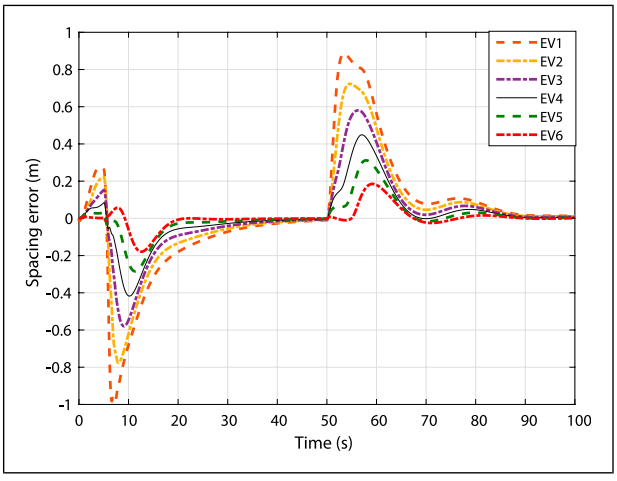

Figure 11. Spacing error versus time plots for a platoon operating in a downhill road, $\mu = 0.5$, $l_{fbi} = 0$ and laden case.

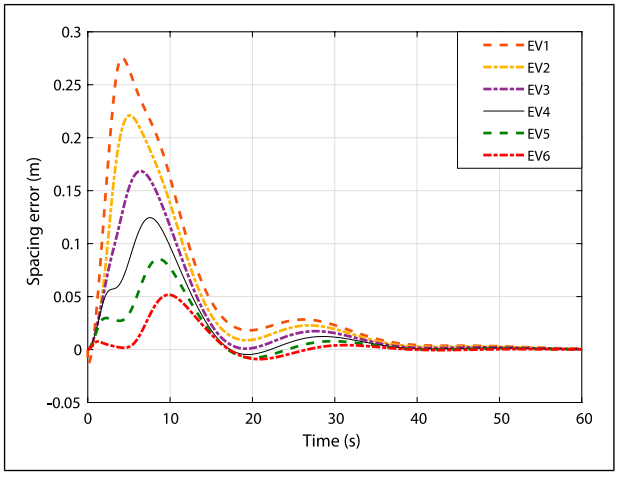

Figure 10. Spacing error versus time plots for a platoon operating in a straight and level road, $\mu = 0.8$, $l_{fbi} = L_i/2$ and laden case.

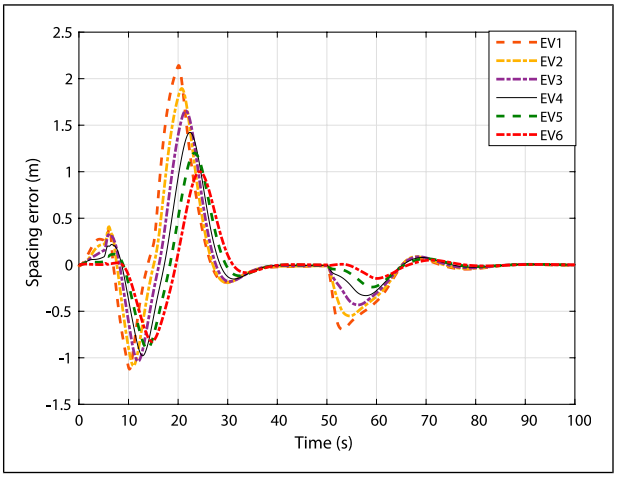

Figure 12. Spacing error versus time plots for a platoon operating in an uphill road, $\mu = 0.5$, $l_{fbi} = L$ and laden case.

Table 4. Sensitivity of battery location on string stability for different operating conditions.

Load	Road gradient	Speed	Dry/wet	
Laden	Straight	Constant	⇓	⇓
		Perturbation	⇓	⇓
	Downhill	Constant	⇓	⇑
		Perturbation	⇔	⇑
	Uphill	Constant	⇓	⇔
		Perturbation	⇔	⇑
Unladen	Straight	Constant	⇓	⇓
		Perturbation	⇔	⇑
	Downhill	Constant	⇔	⇑
		Perturbation	⇑	⇑
	Uphill	Constant	⇔	⇑
		Perturbation	⇑	⇑

⇓: low sensitivity; ⇔: medium sensitivity; ⇑: high sensitivity.

spacing errors. Under such an assumption, the proposed CTH–based SMC controller resulted in string stable operation during the lead vehicle speed perturbation manoeuvre. However, there would be scenarios with non-zero velocity and spacing errors during real platoon operations. This would be investigated as part of future research.

7. Conclusion

In this study, an attempt is made for the controller design and analysis of electric HCRV platoons. To ensure a stable collision-free operation under various operating conditions, a string stable controller using SMC has been proposed. An electric HCRV platoon has been modelled incorporating both pneumatic and electric actuator dynamics, resistive forces, nonlinear MF tyre model, wheel dynamics and different battery pack positions. The effect of three distinct battery pack locations on the electric HCRV platoon stability under different operating conditions was analysed. The platoon was found to be having varying degrees of sensitivity to change in battery locations. The observations regarding this are summarised in Table 4.

If it is possible to know the route and drive cycle beforehand, then observations from this study can be used as a pointer to choose battery placement location for the electric HCRV platoon to have a safe and collision-free operation. For instance, for a drive cycle with majority climbing roads, it would be advised to keep the battery pack near the rear wheels to ensure a stable platoon operation.

Even though PRERL has been shown to have reduced reaching phase duration compared with conventional reaching law structures, the existence of reaching phase before establishing sliding phase is still an important consideration. If an external disturbance happens to affect the platoon during the reaching phase, it could lead to string instability. To address this issue, SMC design methodologies that would further reduce the impact of the reaching phase would be investigated in the future work.

Declaration of Conflicting Interests

The author(s) declared no potential conflicts of interest with respect to the research, authorship and/or publication of this article.

Funding

The author(s) disclosed receipt of the following financial support for the research, authorship and/or publication of this article: The authors thank the Ministry of Skill Development and Entrepreneurship, Government of India, for funding through the grant EDD/14–15/023/MOL/NILE.

ORCID iDs

K B Devika https://orcid.org/0000-0003-0600-1218
Rohith G https://orcid.org/0000-0001-9678-9365
Shankar C Subramanian https://orcid.org/0000-0001-6710-2202

References

Alam A, Besselink B, Turri V, et al. (2015) Heavy-duty vehicle platooning for sustainable freight transportation: a cooperative method to enhance safety and efficiency. *IEEE Control Systems Magazine* 35(6): 34–56.

Automotive, IPG (2018) *IPG Truckmaker® Reference Manual*. version 7.0.

Cano ZP, Banham D, Ye S, et al. (2018) Batteries and fuel cells for emerging electric vehicle markets. *Nature Energy* 3(4): 279–289.

Chehardoli H (2020a) Robust optimal control and identification of adaptive cruise control systems in the presence of time delay and parameter uncertainties. *Journal of Vibration and Control* 26(17–18): 1590–1601. doi: 10.1177/1077546319901086

Chehardoli H (2020b) Multi look-ahead consensus of vehicular networks in the presence of random data missing. *Journal of Vibration and Control*. doi: 10.1177/1077546320933465

Chehardoli H and Ghasemi A (2019) Formation control of longitudinal vehicular platoons under generic network topology with heterogeneous time delays. *Journal of Vibration and Control* 25(3): 655–665.

Devika KB and Thomas S (2017) Power rate exponential reaching law for enhanced performance of sliding mode control. *International Journal of Control, Automation and Systems* 15(6): 2636–2645.

Devika KB, Sridhar N, Yellapantula VRS, et al. (2019) Control of heavy road vehicle platoons incorporating actuation dynamics. In: TENCON 2019-2019 IEEE region 10 conference (TENCON), Kochi, India, October 2019, 1434–1439. IEEE.

Ehsani M, Gao Y, Longo S, et al. (2018) *Modern Electric, Hybrid Electric, and Fuel Cell Vehicles*. Boca Ranton, FL: CRC Press.

Guo X, Wang J, Liao F, et al. (2016) Distributed adaptive integrated-sliding-mode controller synthesis for string stability of vehicle platoons. *IEEE Transactions on Intelligent Transportation Systems* 17(9): 2419–2429.

Hussein AA and Rakha HA (2020) *Vehicle Platooning Impact on Drag Coefficients and Energy/fuel Saving Implications*.arXiv preprint arXiv:2001.00560.

Kaluva ST, Pathak A and Ongel A (2020) Aerodynamic drag analysis of autonomous electric vehicle platoons. *Energies* 13(15): 4028.

Kwon J-W and Chwa D (2014) Adaptive bidirectional platoon control using a coupled sliding mode control method. *IEEE Transactions on Intelligent Transportation Systems* 15(5): 2040–2048.

Larson J, Liang KY and Johansson KH (2014) A distributed framework for coordinated heavy-duty vehicle platooning. *IEEE Transactions on Intelligent Transportation Systems* 16(1): 419–429.

Lv C, Zhang J, Li Y, et al. (2015) Mechanism analysis and evaluation methodology of regenerative braking contribution to energy efficiency improvement of electrified vehicles. *Energy Conversion and Management* 92: 469–482.

Mulholland E, Teter J, Cazzola P, et al. (2018) The long haul towards decarbonising road freight - a global assessment to 2050. *Applied Energy* 216: 678–693.

Na G, Park G, Turri V, et al. (2020) Disturbance observer approach for fuel-efficient heavy-duty vehicle platooning. *Vehicle System Dynamics* 58(5): 748–767.

Pacejka H (2005) *Tire and Vehicle Dynamics*. Oxford, UK: Elsevier.

Sridhar N, Subramaniyam KV, Subramanian SC, et al. (2017) Model based control of heavy road vehicle brakes for active safety applications. In: 2017 14th IEEE India council international conference (INDICON), Roorkee, India, 11 October 2018, pp. 1–6. IEEE.

Subramaniyam KV and Subramanian SC (2019) Impact of regenerative braking torque blend-out characteristics on electrified heavy road vehicle braking performance. *Vehicle System Dynamics* 59(2): 1–26.

Suriyamoorthy S, Gupta S, Kumar DP, et al. (2019) Analysis of hub motor configuration and battery placement on ride comfort of electric trucks. In: IEEE vehicle power and propulsion conference (VPPC), Hanoi, Vietnam, 09 January 2020, pp. 1–6. IEEE.

Swaroop D (1997) *String stability of interconnected systems: an application to platooning in automated highway systems*.

Swaroop D, Hedrick JK, Chien CC, et al. (1994) A comparision of spacing and headway control laws for automatically controlled vehicles1. *Vehicle System Dynamics* 23(1): 597–625.

Teoh T, Kunze O, Teo C-C, et al. (2018) Decarbonisation of urban freight transport using electric vehicles and opportunity charging. *Sustainability* 10(9): 3258.

Turri V, Besselink B and Johansson KH (2016) Cooperative look-ahead control for fuel-efficient and safe heavy-duty vehicle platooning. *IEEE Transactions on Control Systems Technology* 25(1): 12–28.

Utkin V (1977) Variable structure systems with sliding modes. *IEEE Transactions on Automatic control* 22(2): 212–222.

Wu Z, Wang C, Wolfram P, et al. (2019) Assessing electric vehicle policy with region-specific carbon footprints. *Applied Energy* 256: 113923.

Yanakiev D and Kanellakopoulos I (1995) Variable time headway for string stability of automated heavy-duty vehicles. In: Proceedings of 1995 34th IEEE conference on decision and control, LA, USA, 06 August 200, *4*, 4077–4081. IEEE.

Yu K, Liang Q, Yang J, et al. (2016a) Model predictive control for hybrid electric vehicle platooning using route information. *Proceedings of the Institution of Mechanical Engineers, Part D: Journal of Automobile Engineering* 230(9): 1273–1285.

Yu K, Yang H, Tan X, et al. (2016b) Model predictive control for hybrid electric vehicle platooning using slope information. *IEEE Transactions on Intelligent Transportation Systems* 17(7): 1894–1909.